Grain Boundary Sliding-Induced Creep of Powder Metallurgically Produced Nb-20Si-23Ti-6Al-3Cr-4Hf

C. Seemüller, M. Heilmaier

Chair of Physical Metallurgy, Institute of Applied Materials, Karlsruhe Institute of Technology, Engelbert-Arnold-Str. 4, 76131 Karlsruhe, Germany

Abstract

The multi-component alloy Nb-20Si-23Ti-6Al-3Cr-4Hf was produced by powder injection molding or hot isostatic pressing of pre-alloyed, gas-atomized powder. The resulting microstructure comprises the Nb solid solution as well as the α- and γ-modifications of Nb_5Si_3. Creep is evaluated in constant true stress tests at 1000 and 1100 °C. The analysis of the creep behavior regarding its dependence on microstructural and testing parameters such as grain size, stress, and temperature reveals grain boundary sliding as the prevalent deformation mechanism. This is backed up by SEM/EBSD and TEM observations in the undeformed and deformed state. This creep mechanism was found to be a direct result of the small grain/phase sizes after powder metallurgical processing and led to a creep resistance even lower than that of a single-phase niobium-based alloy.

Keywords

high-temperature composite, niobium silicon base, creep mechanism, creep strength, grain boundary sliding

1 Introduction

In high temperature applications such as gas turbines, today nickel-base superalloys are commonly employed to fulfill the requirements on high temperature creep strength as well as oxidation resistance and toughness. A further improvement in efficiency of those combustion engines is possible by increasing the turbine inlet temperature or by reducing the density [1]. Niobium-based silicide composites have been researched for some while now to deliver on both of these prospects. Alloys of this class of materials usually contain a niobium solid solution for ductility and toughness at lower temperatures, or more specifically at room temperature, and an Nb_5Si_3 intermetallic phase for high temperature strength. The density of those alloys is typically around 7 $g \cdot cm^{-3}$ which compares favorably with 9 $g \cdot cm^{-3}$ for state of the art nickel-base alloys. The binary system, however, while offering sufficient creep strength [2, 3] suffers from insufficient oxidation resistance [4]. Alloying elements such as titanium, aluminum, and chromium have been added to improve on that [5–8]; hafnium is also oftentimes added for solid solution hardening of the niobium phase [7]. A prominent example of this alloying scheme was the MASC alloy (metal and silicide composite, Nb-16Si-25Ti-2Al-2Cr-8Hf, compositions are given in atomic percent throughout this paper) introduced by Bewlay et al. in 1996 [9]. Those alloys, typically produced via induction skull melting (ISM), arc-melting, or directional solidification (DS), show a good balance of creep and oxidation properties. As segregations are frequently observed during cast metallurgy of this kind of materials [6], castability is often poor, and since near net-shape component production is desirable, powder metallurgy (PM) offers the potential to target all three of these issues. Besides, PM also allows for composition variations

that are inaccessible by cast metallurgy [38]. Therefore, in this work, a MASC-derived composition (Nb-20Si-23Ti-6Al-3Cr-4Hf) was assessed regarding its creep properties and underlying deformation mechanisms after being produced via advanced powder metallurgical techniques.

2 Experimental

Rods of the nominal composition Nb-20Si-23Ti-6Al-3Cr-4Hf were produced by plasma-melting of pure elements. The rods were directly atomized by electrode induction-melting gas atomization (EIGA). The resulting powders were sieved into different size classes of <25, 25-45, 45-106, 106-225, and >225 μm [10]. In this work, it will only be reported on properties of the powder fraction < 25 μm. Compaction of the powders was done via powder injection molding (PIM) or hot isostatic pressing (HIP).

For PIM, the powders were mixed with a polymer wax-based binder to produce a feedstock (powder load of 70 %) and subsequently injection molded into small cylinders. After solvent-based debinding with hexane and thermal debinding at 600 °C, the samples were sintered at 1500 °C for 3 hours. For further details on PIM processing, the reader is referred to [10].

HIP was done at 1230 °C for 4 hours at a pressure of 150 MPa, after the powder was filled in a mild steel can on a vibrating table and evacuated over night before crimping and welding the can shut.

Additionally, monolithic intermetallic phases of α-Nb_5Si_3 and γ-Nb_5Si_3 were produced by traditional non-consumable tungsten electrode arc-melting with compositions of Nb-36.5Si-13Ti-1Al-4Hf and Nb-36Si-23.5Ti-2.5Al-0.5Cr-7.5Hf, respectively. These compositions had been determined by EDS on the separate phases in the compacted composite. To insure homogeneity, buttons were flipped and remelted at least 5 times.

Cuboid samples (4×4×8 mm) were extracted via electro discharge machining (EDM) from HIP cylinders and arc melted buttons.

Heat treatments were performed in a Gero tube furnace under high purity argon flow at 1300 °C for 100 hours, or 1500 °C for 20 or 100 hours.

The resulting sample conditions will be denoted by the compaction process (HIP or PIM) and the heat treatment state (AC for as-consolidated or HT for heat treatment followed by the temperature in centigrade and the duration in hours).

Compressive creep testing was done in a Zwick Z100 electromechanical testing machine with attached Maytec vacuum radiation furnace. Load-deformation feedback control was set up to ensure constant true stress during deformation. Additionally, compression tests on select samples were performed at constant initial strain rates between 10^{-4} s^{-1} to 10^{-2} s^{-1}.

Punch faces of compression samples were grinded plan parallel to a finish of grit P2500 and covered with a thin layer of h-BN to reduce friction between the SiC punches and the samples.

Microstructural analysis was done with a Zeiss Evo 50 scanning electron microscope (SEM) equipped with tungsten filament with energy dispersive X-ray spectrometer (EDS) and for EBSD mappings a Zeiss Auriga SEM with field emission gun was used. X-ray diffraction patterns in this work were recorded with a Bruker D2 Phaser diffractometer with Cu-K_α radiation (λ = 0.15406 nm) and an attached Lynxeye line detector at room temperature to identify the phases present.

3 Results

3.1 Initial Microstructure

In all powder metallurgical cases, the microstructure reveals up to four phases: niobium solid solution (Nb_{ss}), α-Nb_5Si_3, γ-Nb_5Si_3, and HfO_2. They

show up in bright grey, dark grey, medium gray and white contrast in SEM backscatter electron micrographs, respectively. One exception is the HT1300-100 condition, were γ-Nb_5Si_3 appears brighter than Nb_{ss} due to increased solubility of hafnium in this silicide at this temperature. Figure 2 shows the evolution of microstructure with increase in heat treatment duration and temperature. Exemplarily, the diffraction patterns recorded for HIP are given in Figure 1, left.

The arc-melted material is indeed monolithic intermetallic except for a small Nb_{ss}-peak detectable for γ-Nb_5Si_3 (Figure 1 right).

While area fractions of the silicide phases significantly vary depending on heat treatment (α-Nb_5Si_3: 27 – 37 %; γ-Nb_5Si_3: 17 – 27 %), the Nb_{ss} fraction stays constant at around 46 % and HfO_2 is below 1 %. The grain size of HIP and PIM was extracted from EBSD measurements for the HT1300-100 and HT1500-100, and HT1300-100, HT1500-20, and HT1500-100 conditions, respectively (Table 1). Note here that even after a 1500 °C heat treatment, coarsening of the microstructure is rather weak, giving grain/phase sizes of less than 10 µm on average. This indicates sluggish diffusion being a typical signature of RM-based silicide alloys [11, 12].

Table 1

3.2 Creep

Usually, the steady-state strain rate $\dot{\varepsilon}_s$ of a creep experiment in dependence of testing parameters stress σ and temperature T, and the microstructural parameter grain size d_g, is given by the following relationship [13, 14]

$$\dot{\varepsilon}_s(\sigma, T, d_g) = \frac{A \cdot D}{d_g^p} \cdot \sigma^n \cdot \exp\left(\frac{Q_c}{RT}\right) \quad (1)$$

where A is a constant, D the diffusion coefficient for the dominant (i.e. "rate controlling") mechanism, p the grain size exponent, n the stress exponent, Q_c

the activation energy for creep, and R the gas constant. The determination of the material parameters p, n, and Q_c and their implications for creep mechanisms active in the analyzed niobium silicide composite are the main focus in what follows.

However, we will start with the creep curve itself (Figure 3), as it does not show the expected steady-state, i.e. constant, strain rate over a marked amount of plastic strain but rather a minimum creep rate $\dot{\varepsilon}_{\mathrm{m}}$. This can stem from microstructural changes very early during deformation as it is known e.g. for Ni-base superalloys [14], leading to the commencing of the tertiary creep before a steady-state strain rate is reached: in the particular case of Ni-base superalloys the microstructural instability is often called "rafting" [15]. In the present case, the creep rate increase is not linked to microstructural changes as shown later, but rather to damaging. During deformation, phase boundaries fail and cracks propagate along them and into adjacent grains as shown in Figure 3 (right). Equation (1) applies accordingly for the minimum strain rate $\dot{\varepsilon}_{\mathrm{m}}$.

3.3 Stress dependence

Using isothermal creep tests at varying stresses, the stress exponent n can be determined for each sample condition as the slope of a double-logarithmic plot of minimum strain rate over stress (Figure 4 and Figure 5). In Figure 4, also the goal for creep resistance is given as dashed horizontal line (corresponding to < 1 % deformation in 100 – 125 h) as proposed by several researchers familiar with the requirements for aircraft turbines [5, 6, 16, 17]. However, this goal was postulated for temperatures of more than 1200 °C and stresses on the order of 150 MPa. For the present material, this goal is not met even for 1000 °C and 50 MPa. Another pre-requisite, a plastic deformation of less than 0.5 % during primary creep [5] is not met either.

Independent of sample condition or testing temperature, a stress exponent n of about 2 is apparent. This is in a range often observed when grain boundary sliding is the predominant creep mechanism, e.g. in fine-grained (< 10 µm) multi-phase materials [14, p. 411].

3.4 Temperature dependence

By changing the testing temperature at constant stress, the activation energy Q_c is determined as the slope of a $\ln(\dot{\varepsilon}_m)$ over $1/RT$ plot according to the transformation of equation (1) for constant stress and constant grain size (Figure 6).

$$\ln(\dot{\varepsilon}_m) = \ln(A_2) - Q_c \cdot \frac{1}{RT} \tag{2}$$

A_2: constant

As the strain rate is constant only in a small strain regime, testing temperature was changed back to the starting temperature after each measuring temperature for HIP HT1500-100. The control strain rate stayed constant within a standard deviation of 6.4 %, which corresponds to a deviation of 26 kJ·mol^{-1} from the average Q_c value. All measured activation energies lie well in this range of scatter around 400 kJ·mol^{-1}.

3.5 Grain size dependence

During "pure" dislocation creep, the deformation is controlled by a dynamic equilibrium between the formation and annihilation of dislocations in the sub-grains, which limit their mean free path. Even in small grains, dislocation interaction is assumed to mainly take place in the three-dimensional dislocation network. Usually, the observed increase in strain rate for decreasing grain size is a result of grain boundary sliding becoming non-negligible anymore [13].

Another mechanism that will lead to a grain size dependence of creep is the presence of diffusional creep. Nabarro and Herring [18, 19], and Coble [20]

proposed dislocation independent high temperature deformation based on diffusional flow of vacancies through the volume or along the grain boundaries, respectively. This would lead to a grain size exponent p of 2 or 3, respectively, combined with a stress exponent n close to unity (compare equation (1)).

Similar to the so called Norton plots, Figure 4 and Figure 5, the logarithmic strain rate can be plotted over the grain size of different heat treatment conditions to obtain p as the slope (Figure 7). For different testing temperatures and stresses a mean value of the grain size exponent of 4.4 is observed.

4 Discussion

4.1 Microstructural changes

To fully rationalize the deformation mechanisms operating in these multicomponent multiphase materials, changes in microstructural features during deformation such as grain morphology and texture have to be analyzed as well. For that purpose, a heat-treated sample (PIM HT1300-100) was deformed in compression to a true plastic strain of $\varepsilon_t = 1$ (1100 °C, 50 MPa, corresponding to a height reduction by 63 %). The aspect ratio S of the grains is in this case defined as the phase size perpendicular to the loading direction divided by the one parallel to it, as measured by the linear intersect method on optical micrographs. The increase in S due to the deformation compared to the undeformed state is from unity to 1.23 and, thus, hardly significant (Table 2). This is also depicted in EBSD phase maps before and after the deformation (Figure 8).

Table 2

For previously equiaxed grains the expected aspect ratio can be easily estimated for pure dislocation-based deformation (only change in grain shape

without rearrangement of the grains). Under the boundary conditions of constant volume and isotropic strain perpendicular to the loading axis the resulting aspect ratio is given by equation (3), where ε_t is the final true strain. In case of $\varepsilon_t = 1$ a value for S of 4.5 is expected.

$$S = \exp\left(-\frac{3}{2}\varepsilon_t\right) \tag{3}$$

Additionally, EBSD measurements on the same cross-section reveal no significant texture, especially in case of the Nb_{ss}, which would be expected to show the strongest deformation texture due to its ease of deformability under the chosen conditions (Table 3). To the contrary, the highest multiple of uniform distribution (MUD) is reduced for the intermetallic phases. During compression, for the bcc solid solution (Nb_{ss}) the formation of a ⟨111⟩/⟨001⟩ fiber texture parallel to the compression axis is expected [21, p. 192]. This was previously shown by several researchers for pure niobium [22–24]. Vishwanadh et al. [22] found for a similar amount of thickness reduction (60 %) an MUD value above 3 in ⟨111⟩.

Table 3

At the same time, the bulk intermetallic phases (α-Nb_5Si_3 and γ-Nb_5Si_3 produced by arc melting) yield creep rates more than three orders of magnitude lower – at higher stresses – than the composite (Table 4). This is well in line with results obtained for binary and multi-component Nb-based silicides, where γ-Nb_5Si_3 demonstrated to have lower creep strength than α-Nb_5Si_3 [25–28]. This suggests that deformation of the intermetallic compound itself cannot be the rate-controlling factor in the composite's high creep rates.

Table 4

As the grains do not deform, strain has to be obtained by rearrangement of grains, i.e. grain boundary sliding. Another feature of grain boundary sliding,

the coalescence of phases during deformation [29, 30] is found as well (Figure 8). The sliding will induce misfit stresses in the grain boundary triple junctions that have to be accommodated by dislocation or diffusional creep. When those accommodation processes cannot keep up, void formation and eventually cracking of the grain boundaries as shown earlier will occur. The activation energy for creep in this study was found to be 400 ± 26 kJ·mol^{-1}, which reflects the activation energy for the rate controlling accommodation mechanism. This value is in good agreement with the activation energy for niobium self diffusion of 349–440 kJ·mol^{-1} [31–34] and that for diffusion of titanium in niobium 364 kJ·mol^{-1} [35]. Diffusion in Nb_5Si_3, however, requires significantly lower activation energies (201–271 kJ·mol^{-1} [36–38]). TEM investigations have shown the presence of dislocations in the Nb_{ss} after deformation (Figure 9) and the lack thereof before it. Hence, most likely, dislocation movement in the niobium solid solution is the dominant accommodation mechanism. This explains also the observed coalescence of phases, as Nb_{ss} has to participate in the grain displacement with the silicides not being able to accommodate triple junction stresses at the given temperatures. Similar behavior was found by Jéhanno et al. [11, 39] in molybdenum-based silicide composites. In this case, the grain size exponent p was close to unity, though, confirming accommodation by dislocations [40, 41]. The grain size exponent found in the present work (4.4) is out of range even for grain boundary diffusion as main accommodation mechanism ($p \approx 3$), which can be excluded based on the activation energy.

4.2 Critical grain size

Grain boundary sliding will become the dominant creep mechanism, when the stress dependent sub-grain size d_{sg} that forms during the primary stage of creep becomes larger than the grain size d_g [13, p. 225] and the necessary

dislocation interactions cannot take place anymore in the sub-grain boundaries.

$$d_{\mathrm{sg}} \sim \frac{Gb}{\sigma} \tag{4}$$

G: shear modulus

b: Burgers vector

Hence, a transition stress σ_{trans} can be defined for $d_{\mathrm{sg}} = d_{\mathrm{g}}$ at which the deformation mode changes from dislocation creep (high stresses) to grain boundary sliding dominated creep (low stresses). To explore the former regime, constant strain rate tests have been performed where the maximum true stress corresponds to the creep stress that would have to be applied to achieve this strain rate as $\dot{\varepsilon}_m$ in a constant stress experiment. However, at those strain rates, a constant strain rate compression test is better to control. In Figure 10 the 1000 °C creep data is accompanied by the results of those tests.

While the grain size dependence does not completely disappear for high stresses where dislocation creep appears to be rate controlling ($n = 5$), it is much less pronounced than in the GBS regime. Even though constant strain rate tests were performed only on AC and HT1500-100 material, transition stresses can be estimated as 230, 190, and 145 MPa for HT1300-100, HT1500-20, and HT1500-100 heat treatment conditions, respectively. If plotted over the inverse grain size, the linear relationship seen in Figure 11 is expected. For the above-mentioned application stress of 150 MPa some coarsening would be necessary to lie well within the dislocation creep regime. A further increase in temperature, e.g. to the postulated 1200 °C and above would require even more pronounced coarsening. Given that a heat treatment of 1500 °C for 100 h barely doubled the grain size and that coarsening is proportional to the square root of time, this would likely be not feasible.

5 Conclusions

A multi-component Nb-Si composite (Nb-20Si-23Ti-6Al-3Cr-4Hf) has been produced by powder metallurgical means, i.e. powder injection molding or hot isostatic pressing of pre-alloyed gas-atomized powders. The processing led to a fine-grained microstructure that could be coarsened by heat treatments as high as 1500 °C to a grain/phase size of ≈10 μm.

In general, creep performance was not sufficient to be a viable alternative for current turbine solutions. The main reason being that the creep behavior is characterized by grain boundary sliding over the whole range of stresses and temperatures applied. Based on the activation energy of 400 kJ·mol^{-1} and the observation of dislocations inside the solid solution grains after high temperature deformation, deformation accommodation in grain boundary triple junctions by dislocations is likely to be dominant (compared to accommodation by diffusional creep). Only for very high strain rates (≥ 10^{-3} s^{-1}) a transition to a dislocation-controlled creep deformation could be observed ($n = 5$). By determining a transition stress for different grain sizes, a minimum grain size could be deduced, where dislocation creep would be active at 1000 °C and in a stress regime which is closer to application ≈ 100 MPa. This critical grain size should exceed 20 μm, which is, however, not achievable economically by heat treatment coarsening for the present material.

6 Acknowledgments

This work was financed by the European Union within the HYSOP project (Framework Programme 7, grant no.: 266214). Particular thanks are dedicated to Dr. Nicolas Adkins and Mick Wickins from the University of Birmingham, and Dr. Thomas Hartwig und Marco Mulser from Fraunhofer Institute for

Manufacturing Technology and Advanced Materials, Bremen, for providing the sample material.

We acknowledge the Karlsruhe Nano Micro Facility (KNMF, www.kit.edu/knmf) of the Forschungszentrum Karlsruhe for provision of access to instruments at their laboratories and we would like to thank Dr. Alexander Kauffmann for assistance in using the Laboratory for Microscopy and Spectroscopy.

7 References

[1] J.H. Perepezko, "The Hotter the Engine, the Better", *Science*, vol. **326**, no. 5956, pp. 1068–1069, 2009.

[2] I. Weiss, M. Thirukkonda, and R. Srinivasan, "Effect of Deformation Processing on Mechanical Properties of Nb-10 a/o Si In-Situ Composite", *Mater. Res. Soc. Symp. Proc.*, vol. **322**, pp. 377–386, 1994.

[3] P.R. Subramanian, M.G. Mendiratta, and D.M. Dimiduk, "Microstructures and Mechanical Behavior of Nb-Ti Base Beta + Silicide Alloys", *Mater. Res. Soc. Symp. Proc.*, vol. **322**, pp. 491–502, 1994.

[4] M. Bachmann, "Herstellung und Oxidation von Niobsilizid-Legierungen", Diplom Thesis, Technische Universität Darmstadt, 2012.

[5] B.P. Bewlay, M.R. Jackson, J.-C. Zhao, and P.R. Subramanian, "A review of very-high-temperature Nb-silicide-based composites", *Metall. Mater. Trans. A*, vol. **34**, no. 10, pp. 2043–2052, 2003.

[6] B.P. Bewlay, M.R. Jackson, J.-C. Zhao, P.R. Subramanian, M.G. Mendiratta, and J.J. Lewandowski, "Ultrahigh-Temperature Nb-Silicide-Based Composites", *MRS Bull.*, vol. **28**, no. 9, pp. 646–653, 2003.

[7] B.P. Bewlay, M.R. Jackson, and M.F.X. Gigliotti, "Niobium Silicide High Temperature In Situ Composites", in *Intermetallic Compounds - Principles and Practice*, vol. **3**, J. H. Westbrook and R. L. Fleischer, Eds. Chichester, UK: John Wiley & Sons, Ltd, 2002, pp. 541–560.

[8] R. Mitra, "Mechanical behaviour and oxidation resistance of structural silicides", *Int. Mater. Rev.*, vol. **51**, no. 1, pp. 13–64, 2006.

[9] B.P. Bewlay, M.R. Jackson, and H.A. Lipsitt, "The balance of mechanical and environmental properties of a multielement niobium-niobium silicide-based in situ composite", *Metall. Mater. Trans. A*, vol. **27**, no. 12, pp. 3801–3808, 1996.

[10] M. Mulser, T. Hartwig, C. Seemüller, M. Heilmaier, N. Adkins, and M. Wickins, "Influence of the processing technique on the properties of Nb-Si intermetallic composites for high-temperature applications processed by MIM and HIP", *Adv. Powder Metall. Part. Mater.*, vol. **4**, pp. 8–16, 2014.

[11] P. Jéhanno, M. Heilmaier, H. Saage, M. Böning, H. Kestler, J. Freudenberger, and S. Drawin, "Assessment of the high temperature deformation behavior of molybdenum silicide alloys", *Mater. Sci. Eng. A*, vol. **463**, no. 1–2, pp. 216–223, 2007.

[12] P. Jéhanno, M. Heilmaier, H. Kestler, M. Boning, A. Venskutonis, B. Bewlay, and M. Jackson, "Assessment of a powder metallurgical processing route for refractory metal silicide alloys", *Metall. Mater. Trans. A*, vol. **36**, no. 3, pp. 515–523, 2005.

[13] B. Ilschner, *Hochtemperatur-Plastizität*. Berlin/Heidelberg: Springer-Verlag, 1973.

[14] H. Mughrabi, Ed., *Plastic deformation and fracture of materials*, vol. **6**. Weinheim New York Basel Cambridge: VCH, 1993.

[15] M. Kamaraj, "Rafting in single crystal nickel-base superalloys — An overview", *Sadhana – Acad Proc Eng Sci*, vol. **28**, no. 1–2, pp. 115–128, 2003.

[16] P.R. Subramanian, M.G. Mendiratta, and D.M. Dimiduk, "The development of Nb-based advanced intermetallic alloys for structural applications", *JOM*, vol. **48**, no. 1, pp. 33–38, 1996.

[17] P.R. Subramanian, M.G. Mendiratta, D.M. Dimiduk, and M.A. Stucke, "Advanced intermetallic alloys—beyond gamma titanium aluminides", *Mater. Sci. Eng. A*, vol. **239–240**, pp. 1–13, 1997.

[18] F.R.N. Nabarro, in *Report of a Conference on the Strength of Solids*, London: Physical Society, 1948, p. 75.

[19] C. Herring, "Diffusional viscosity of a polycrystalline solid", *J. Appl. Phys.*, vol. **21**, no. 5, p. 437, 1950.

[20] R.L. Coble, "A model for boundary diffusion controlled creep in polycrystalline materials", *J. Appl. Phys.*, vol. **34**, no. 6, p. 1679, 1963.

[21] U.F. Kocks, C.N. Tomé, H.-R. Wenk, A.D. Rollet, and S.I. Wright, "Typical Textures in Metals", in *Texture and Anisotropy: Preferred Orientations in Polycrystals and Their Effect on Materials Properties*, Cambridge, UK: Cambridge University Press, 1998, pp. 178–239.

[22] B. Vishwanadh, K.V. Mani Krishna, A.K. Revelly, I. Samjdar, R. Tewari, and G.K. Dey, "Textural and microstructural evolutions during deformation and annealing of Nb–1% Zr–0.1% C (wt%) alloy", *Mater. Sci. Eng. A*, vol. **585**, pp. 343–355, 2013.

[23] D. Raabe and K. Lücke, "Rolling and Annealing Textures of BCC Metals", *Mater. Sci. Forum*, vol. **157–162**, pp. 597–610, 1994.

[24] H.F.G. Abreu, S.S.M. Tavares, S.S. Carvalho, T.H.T. Eduardo, A.D.S. Bruno, and M.H. Prado da Silva, "Texture and Microstructure of Cold Rolled and Recrystallized Pure Niobium", *Mater. Sci. Forum*, vol. **539–543**, pp. 3436–3441, 2007.

[25] B.P. Bewlay, C.L. Briant, E.T. Sylven, and M.R. Jackson, "The effects of substitutional additions on creep behavior of tetragonal and hexagonal Nb-silicides", *Mater. Res. Soc. Symp. Proc.*, vol. **753**, p. BB5.24.1-6, 2003.

[26] B.P. Bewlay, C.L. Briant, E.T. Sylven, M.R. Jackson, and G. Xiao, "Creep Studies of Monolithic Phases in Nb-Silicide Based In-Situ Composites", *Mater. Res. Soc. Symp. Proc.*, vol. **646**, p. N2.6.1-6, 2000.

[27] R. Rosenkranz, G. Frommeyer, and W. Smarsly, "Microstructures and Properties of High Melting-Point Intermetallic Ti5si3 and Tisi2 Compounds", *Mater. Sci. Eng. A*, vol. **152**, no. 1–2, pp. 288–294, 1992.

[28] P.R. Subramanian, T.A. Parthasarathy, M.G. Mendiratta, and D.M. Dimiduk, "Compressive creep behavior of Nb5Si3", *Scr. Metall. Mater.*, vol. **32**, no. 8, pp. 1227–1232, 1995.

[29] W. Hotz, E. Ruedl, and P. Schiller, "Observation of processes of superplasticity with the scanning electron microscope", *J. Mater. Sci.*, vol. **10**, no. 11, pp. 2003–2006, 1975.

[30] G.L. Dunlop and D.M.R. Taplin, "A metallographic study of superplasticity in a micrograin aluminium bronze", *J. Mater. Sci.*, vol. **7**, no. 3, pp. 316–324, 1972.

[31] R.E. Einziger, J.N. Mundy, and H.A. Hoff, "Niobium self-diffusion", *Phys. Rev. B*, vol. **17**, no. 2, pp. 440–448, 1978.

[32] D. Ablitzee, "Diffusion of niobium, iron, cobalt, nickel and copper in niobium", *Philos. Mag.*, vol. **35**, no. 5, pp. 1239–1256, 1977.

[33] T.S. Lundy, F.R. Winslow, R.E. Pawel, and C.J. Mchargue, "Diffusion of Nb-95 and Ta-182 in Niobium (columbium)", *Trans. Metall. Soc. Aime*, vol. **233**, no. 8, pp. 1533–1539, 1965.

[34] R. Resnick and L. Castleman, "The Self-Diffusion of Columbium", *Trans. Am. Inst. Min. Metall. Eng.*, vol. **218**, no. 2, pp. 307–310, 1960.

[35] J. Pelleg, "Diffusion of 44Ti into niobium single crystals", *Philos. Mag.*, vol. **21**, no. 172, pp. 735–742, 1970.

[36] S. Prasad and A. Paul, "Growth mechanism of phases by interdiffusion and diffusion of species in the niobium–silicon system", *Acta Mater.*, vol. **59**, no. 4, pp. 1577–1585, 2011.

[37] C. Milanese, V. Buscaglia, F. Maglia, and U. Anselmi-Tamburini, "Reactive growth of niobium silicides in bulk diffusion couples", *Acta Mater.*, vol. **51**, no. 16, pp. 4837–4846, 2003.

[38] E. Fitzer and F.K. Schmidt, "Die Diffusion von Silizium in Nb5Si3", *Monatshefte Für Chem. Chem. Mon.*, vol. **102**, no. 5, pp. 1608–1625, 1971.

[39] P. Jéhanno, M. Heilmaier, H. Saage, H. Heyse, M. Boening, H. Kestler, and J.H. Schneibel, "Superplasticity of a multiphase refractory Mo-Si-B alloy", *Scr. Mater.*, vol. **55**, no. 6, pp. 525–528, 2006.

[40] O.A. Ruano and O.D. Sherby, "Low stress creep of fine-grained materials at intermediate temperatures: Diffusional creep or grain boundary sliding?", *Mater. Sci. Eng.*, vol. **56**, no. 2, pp. 167–175, 1982.

[41] R. Bürgel, H.-J. Maier, and T. Niendorf, *Handbuch Hochtemperatur-Werkstofftechnik : Grundlagen, Werkstoffbeanspruchungen, Hochtemperaturlegierungen und -beschichtungen*, 4th ed. Wiesbaden: Vieweg+Teubner Verlag, 2011.

Figure 1: XRD pattern for HIP AC and heat-treated conditions (left) and arc-melted monolithic intermetallics α-Nb_5Si_3 and γ-Nb_5Si_3 (right).

Figure 2: Backscatter electron micrographs (SEM) of AC and heat-treated conditions of HIP (top) and PIM (bottom) samples.

Table 1: Phase and grain sizes of undeformed HIP and PIM samples for different heat treatment conditions on a cross-section determined by EBSD.

Figure 3: Typical creep curve for the investigated material (left), TEM micrographs (scanning) showing phase boundary cracking after 15 % of plastic deformation (right).

Figure 4: Plot of minimum strain rate over applied true stress at testing temperature of 1000 °C for material produced by HIP or PIM from gas-atomized powders in the AC and heat-treated conditions; the dashed line indicates the creep goal for 1200 °C and stresses of 150 MPa.

Figure 5: Plot of minimum strain rate over applied true stress at testing temperature of 1100 °C for material produced by HIP or PIM from gas-atomized powders in the AC and heat-treated conditions, respectively.

Figure 6: Temperature dependence of strain rate for select sample conditions to determine activation energy for creep.

Figure 7: Double logarithmic plot of creep rate over grain size for PIM ; grain sizes of 4.7, 6.0, and 8.9 μm correspond to the heat treatments HT1300-100, HT1500-20, and HT1500-100, respectively.

Table 2: Phase sizes of deformed and undeformed PIM HT1300-100 on a cross-section determined by the linear intersect method.

Table 3: Inverse pole figures for the three main phases of undeformed and deformed PIM HT1300-100; colors indicate multiples of the uniform distribution (MUD) parallel to the compression direction.

Table 4: Minimum creep rates obtained for monolithic silicides α-Nb_5Si_3 and γ-Nb_5Si_3 at 200 MPa in s^{-1}.

Figure 8: EBSD phase map of PIM HT1300-100 before (left) and after (right) deformation to $\varepsilon_t = 1$, Nb_{ss} in red, α-Nb_5Si_3 in blue, γ-Nb_5Si_3 in green; low angle grain boundaries (2 – 15°) in grey, high angle grain boundaries (> 15°) in black; image width 80 μm, each

Figure 9: TEM micrographs (dark field) of solid solution grains showing dislocations after 15 % of deformation.

Figure 10: Creep data from Figure 4 with constant strain rate results (dotted symbols) for a testing temperature of 1000 °C.

Figure 11: Inverse grain size over transition stress for grain boundary sliding.

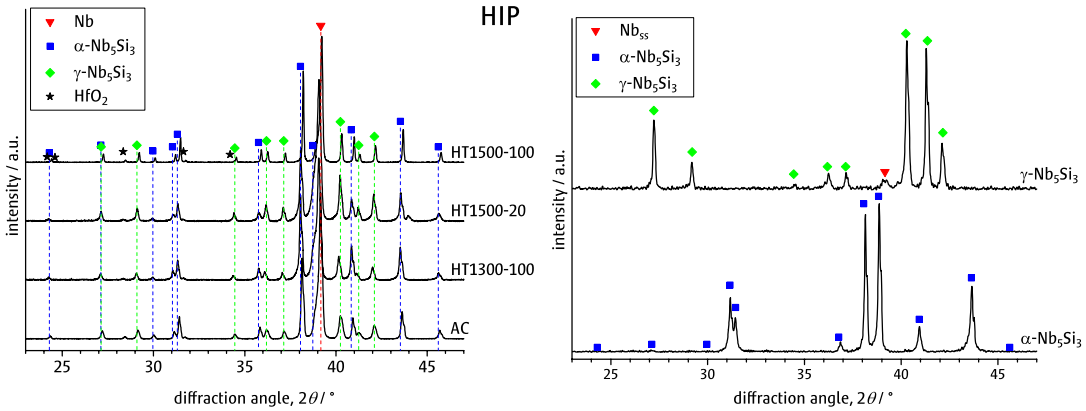

Figure 1: XRD pattern for HIP AC and heat-treated conditions (left) and arc-melted monolithic intermetallics α-Nb5Si3 and γ-Nb5Si3 (right).
Black and white in print

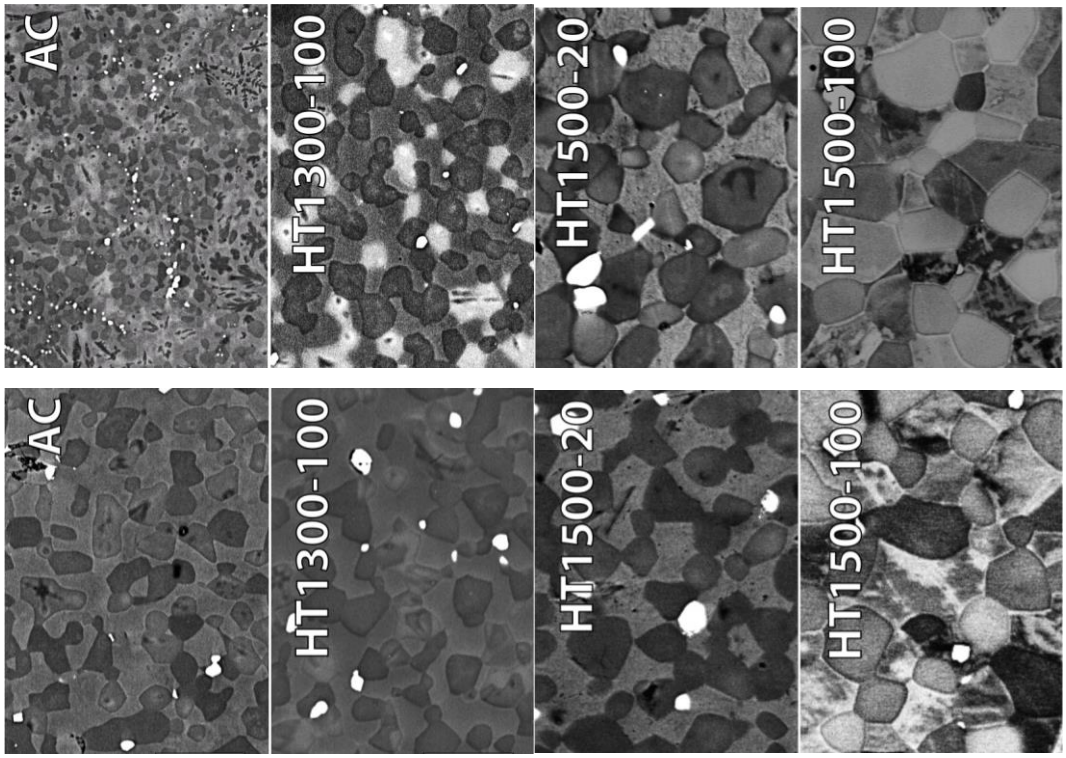

Figure 2: Evolution of microstructure from as-compacted (AC) to different heat-treated conditions for HIP (top) and PIM (bottom) samples (backscatter electron contrast (SEM).

Black and white in print

Table 1: Phase and grain sizes of undeformed HIP and PIM samples for different heat treatment conditions on a cross-section determined by EBSD.

	HIP		**PIM**		
	HT1300-100	**HT1500-100**	**HT1300-100**	**HT1500-20**	**HT1500-100**
mean grain size d_g / µm	3.6 ± 1.4	8.8 ± 3.9	4.7 ± 1.7	6.2 ± 2.1	8.9 ± 3.0

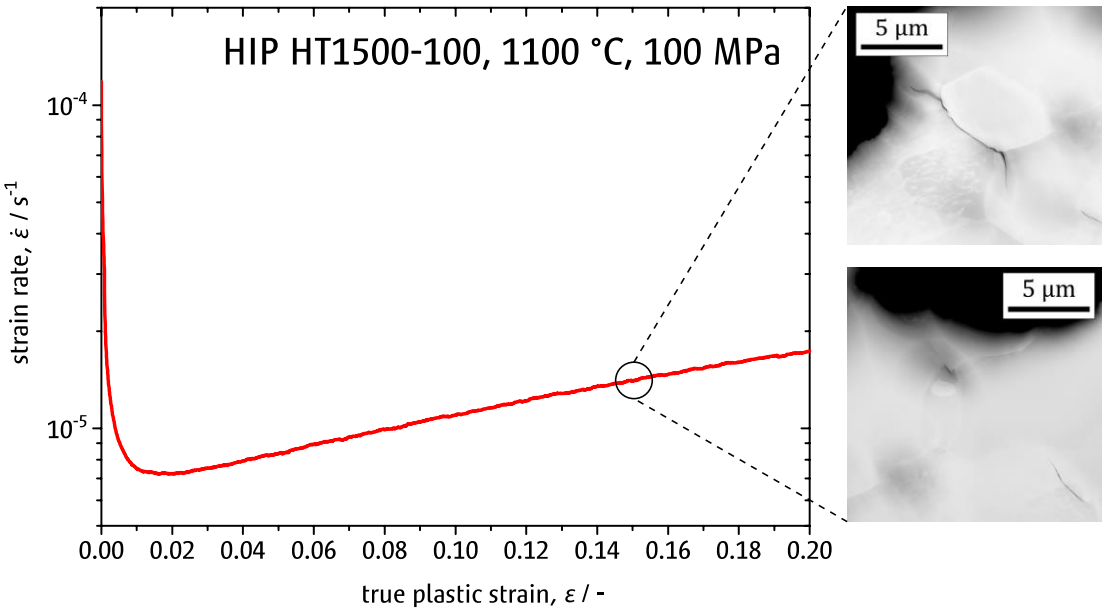

Figure 3: Typical creep curve for the investigated material (left), TEM micrographs (scanning) showing phase boundary cracking after 15 % of plastic deformation (right).

Black and white in print

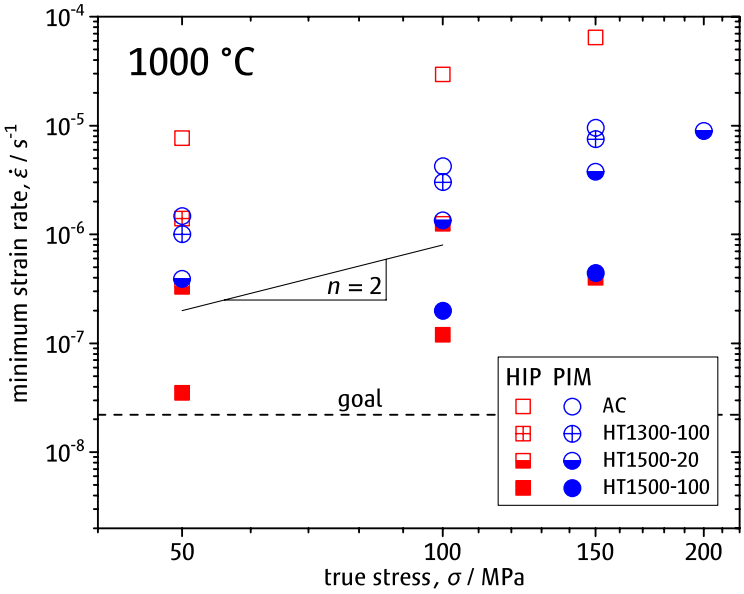

Figure 4: Plot of minimum strain rate over applied true stress at testing temperature of 1000 °C for material produced by HIP or PIM from gas-atomized powders in the AC and heat-treated conditions; the dashed line indicates the creep goal for 1200 °C and stresses of 150 MPa.

Black and white in print

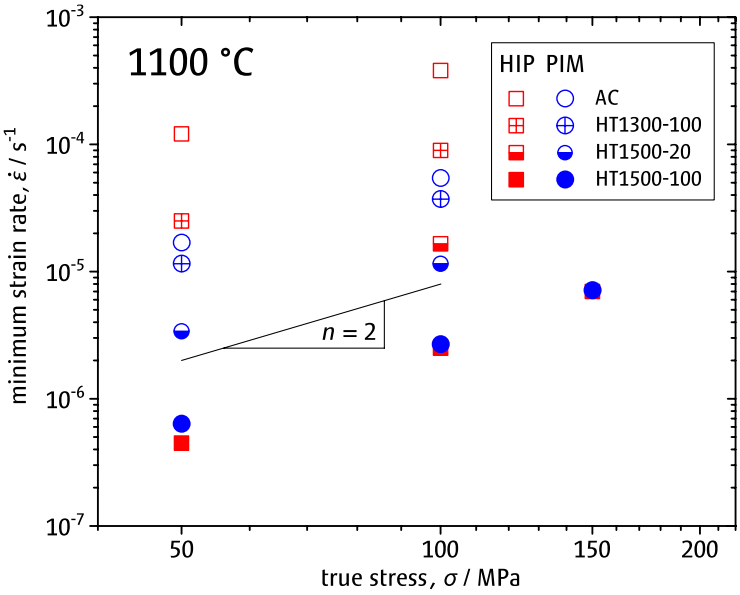

Figure 5: Plot of minimum strain rate over applied true stress at testing temperature of 1100 °C for material produced by HIP or PIM from gas-atomized powders in the AC and heat-treated conditions, respectively.

Black and white in print

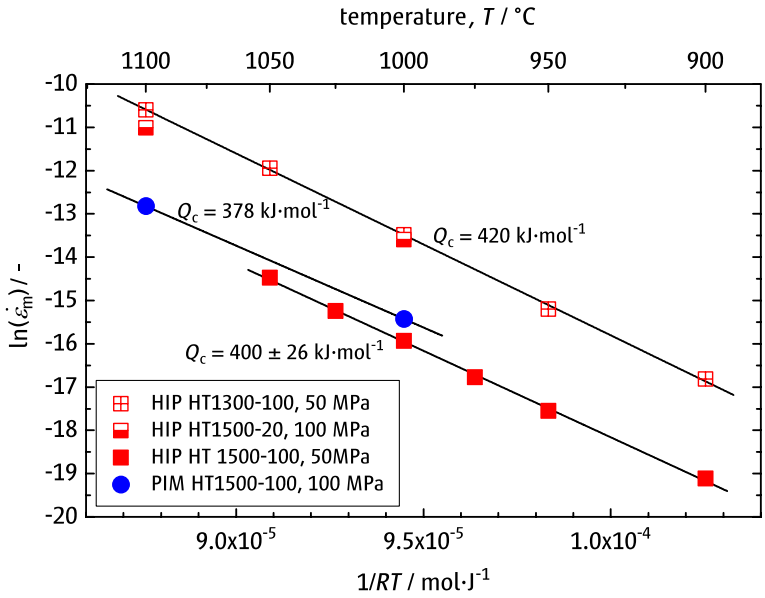

Figure 6: Temperature dependence of strain rate for select sample conditions to determine activation energy for creep.

Black and white in print

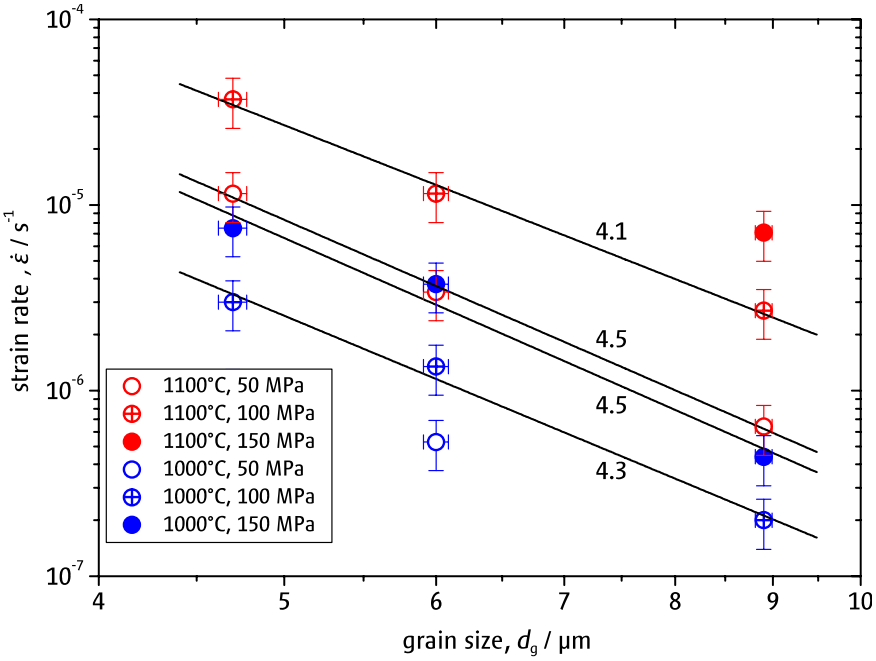

Figure 7: Double logarithmic plot of creep rate over grain size for PIM ; grain sizes of 4.7, 6.0, and 8.9 µm correspond to the heat treatments HT1300-100, HT1500-20, and HT1500-100, respectively.

Black and white in print

Table 2: Phase sizes of deformed and undeformed PIM HT1300-100 on a cross-section determined by the linear intersect method.

phase size / μm	$\boldsymbol{\varepsilon_t = 0}$	$\boldsymbol{\varepsilon_t = 1}$
∥ to loading axis	4.01 ± 0.13	3.59 ± 0.16
⊥ to loading axis	3.94 ± 0.05	4.39 ± 0.33
aspect ratio *S*	1.00 ± 0.03	1.23 ± 0.15

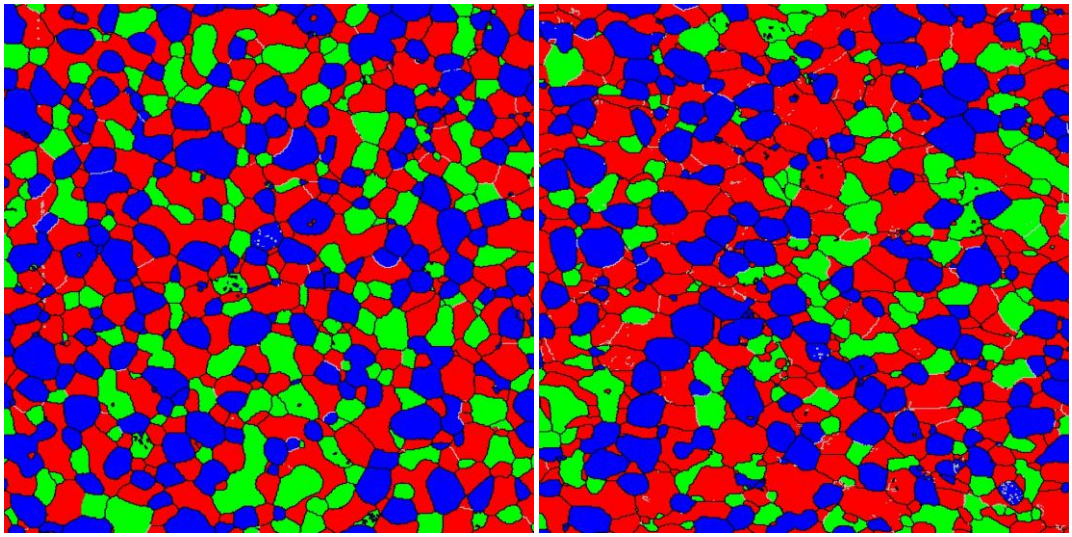

Figure 8: EBSD phase map of PIM HT1300-100 before (left) and after (right) deformation to $\varepsilon_t = 1$, compression direction parallel to vertical edge. Nb_{ss} in red, α-Nb_5Si_3 in blue, γ-Nb_5Si_3 in green; low angle grain boundaries (2 – 15°) in grey, high angle grain boundaries (> 15°) in black; image width 80 µm, each. For colors please refer to the online version.

Black and white in print

Table 3: Inverse pole figures for the three main phases of undeformed and deformed PIM HT1300-100; colors indicate multiples of the uniform distribution (MUD) parallel to the compression direction.

	$\varepsilon_t = 0$	$\varepsilon_t = 1$	MUD
Nb_{ss}	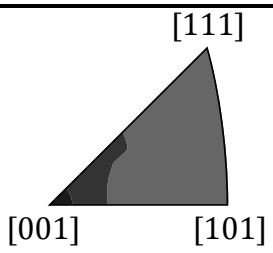	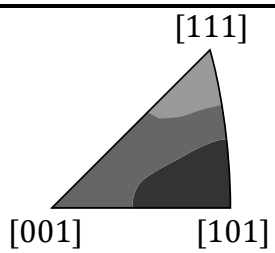	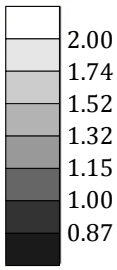
α-Nb_5Si_3	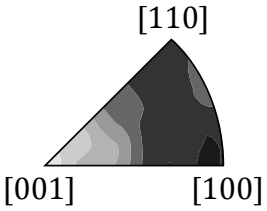	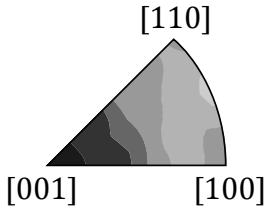	
γ-Nb_5Si_3	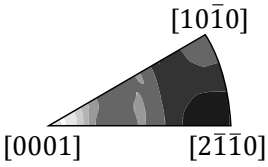	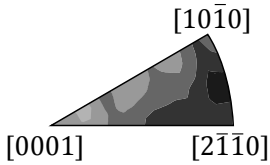	

Black and white in print

Table 4: Minimum creep rates $\dot{\varepsilon}_m$ obtained for monolithic silicides α-Nb5Si3 and γ-Nb5Si3 at 200 MPa in s^{-1}.

temperature / °C	**α-Nb_5Si_3**	**γ-Nb_5Si_3**
1100	$< 1 \cdot 10^{-9}$	$< 1 \cdot 10^{-9}$
1200	—	$2.3 \cdot 10^{-9}$
1300	—	$1.4 \cdot 10^{-8}$

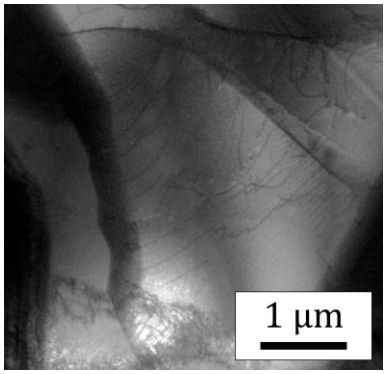

Figure 9: TEM micrograph (dark field) of solid solution grain showing dislocations after 15 % of deformation.

Black and white in print

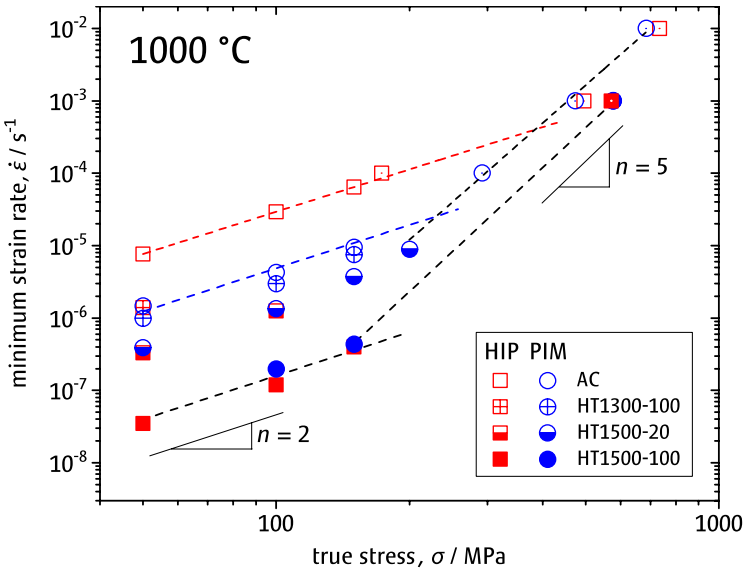

Figure 10: Creep data from Figure 4 with constant strain rate results (dotted symbols) for a testing temperature of 1000 °C.

Black and white in print

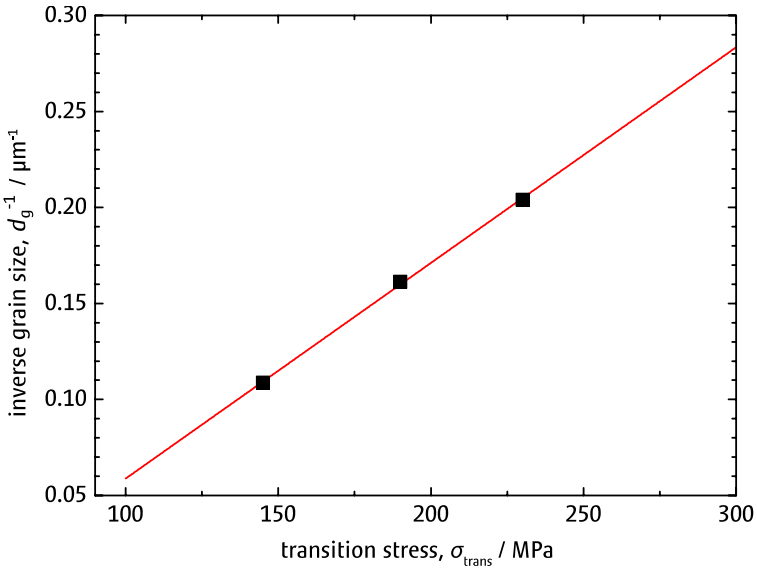

Figure 11: Inverse grain size over transition stress for grain boundary sliding. Black and white in print